Transparent silica aerogel slabs synthesized from nanoparticle colloidal suspensions at near ambient conditions on omniphobic liquid substrates

Michal Marszewski [a,1], Sophia C. King [b], Tiphaine Galy [a], Glareh N. Kashanchi [b], Ali Dashti [a], Yan Yan [b], Man Li [a], Danielle M. Butts [c], Patricia E. McNeil [c], Esther Lan [c], Bruce Dunn [c,d], Yongjie Hu [a], Sarah H. Tolbert [b,c,d], Laurent Pilon [a,d,e,*]

[a] Mechanical and Aerospace Engineering Department, University of California, Los Angeles, Los Angeles, CA 90095, USA
[b] Department of Chemistry and Biochemistry, University of California, Los Angeles, Los Angeles, CA 90095, USA
[c] Department of Materials Science and Engineering, University of California, Los Angeles, Los Angeles, CA 90095, USA
[d] California NanoSystems Institute, University of California, Los Angeles, Los Angeles, CA 90095, USA
[e] Institute of the Environment and Sustainability, University of California, Los Angeles, Los Angeles, CA 90095, USA

HIGHLIGHTS

- Silica aerogels were synthesized on liquid substrates from silica nanoparticles.
- Novel method produced large and thick monoliths at ambient conditions.
- Combination of aging, solvent exchange, and ambient drying ensured large porosity.
- Aerogel monoliths featured high visible transmittance and low thermal conductivity.

GRAPHICAL ABSTRACT
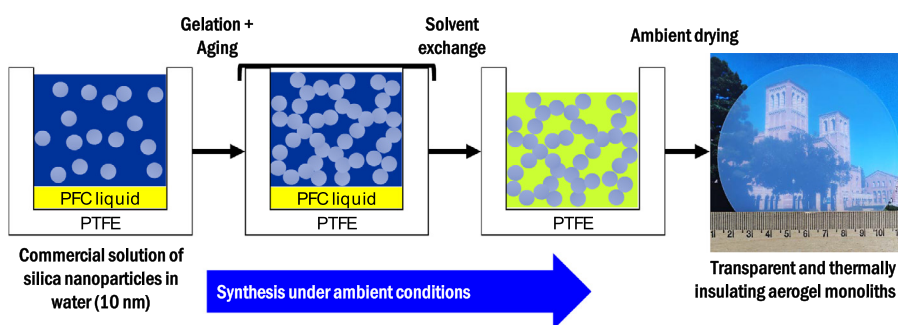
ARTICLE INFO

ABSTRACT

This paper presents a novel sol-gel method to synthesize large and thick silica aerogel monoliths at near ambient conditions using a commercial aqueous solution of colloidal silica nanoparticles as building blocks. To achieve slabs with high visible transmittance and low thermal conductivity, the method combines the strategies of (i) synthesizing gels on an omniphobic perfluorocarbon liquid substrate, (ii) aging at temperatures above room temperature, and (iii) performing solvent exchange with a low-surface-tension organic solvent prior to ambient drying. The omniphobic liquid substrates were used to prevent cracking and ensure an optically-smooth surface, while nanoparticle building blocks were small (<10 nm) to limit volumetric light scattering. Gels were aged at temperatures between 25 and 80 °C for up to 21 days to make them stronger and stiffer and to reduce shrinkage and cracking during ambient drying. Ambient drying was achieved by first exchanging water in the gel pores for octane, followed by drying in an octane-rich atmosphere to decrease capillary forces. The synthesized nanoparticle-based silica aerogel monoliths had thicknesses up to 5 mm, diameters up to 10 cm, porosities exceeding 80%, and thermal conductivities as low as 0.08 W m^{-1} K^{-1}. Notably, the slabs featured visible transmittance exceeding 75% even for slabs as thick as 5 mm. The as-synthesized aerogel monoliths were exposed to TMCS vapor to induce hydrophobic properties resulting in a water contact angle of 140° that prevented water infiltration into the pores and protected the aerogels from water damage. This simple synthesis route conducted at near ambient conditions produces hydrophobic aerogel monoliths with promising optically

---

* Corresponding author at: University of California, Los Angeles, 420 Westwood Plaza, Los Angeles, CA 90095, USA.
  E-mail address: pilon@seas.ucla.edu (L. Pilon).
[1] Present address: Department of Chemistry and Biochemistry, University of Toledo, Toledo, OH 43606, USA.

transparent and thermally insulating properties that can be adhered to glass panes for window insulation and solar-thermal energy conversion applications.

Nomenclature

a	amount adsorbed (cm^3 STP g^{-1})
A_m	surface area of the hot plate inner section (m^2)
$B_{nh,\lambda}$	spectral normal-hemispherical baseline signal (%)
CRI	color rendering index
d_{np}	nanoparticle diameter (nm)
d_1, d_2	diameter of Level 1 and 2 scatterers (nm)
d_{np}	average nanoparticle diameter (nm)
D	slab diameter (cm)
D_m	mass fractal dimension
$D_{nh,\lambda}$	dark signal (%)
D_s	surface fractal dimension
ΔE	geometrical distance in the CIE 1964 uniform chromaticity space
h_{vis}	visible haze (%)
h_λ	spectral haze (%)
I_m	dissipated current in the hot plate inner section (A)
k_{eff}	effective thermal conductivity (W m^{-1} K^{-1})
L	thickness (mm or m)
$M_{d,\lambda}$	spectral diffuse baseline signal (%)
n	amount adsorbed (mol)
p	pressure (Pa)
p_0	saturation pressure (Pa)
P_λ	photopic spectral luminous efficiency function
P_1, P_2	Porod exponents corresponding to Levels 1 and 2
q	scattering vector (Å^{-1})
Q_m	heat generation rate in the hot plate inner section (W)
R	gas constant (K mol^{-1} K^{-1})
R_{g1}, R_{g2}	Gyration radii corresponding to Levels 1 and 2 (nm)

R_m	resistance of the wires embedded in the hot plate inner section (Ω)
S_{BET}	specific surface area (m^2 g^{-1})
S_{BET}	average specific surface area (m^2 g^{-1})
$S_{d,\lambda}$	spectral diffuse transmitted signal (%)
$S_{nh,\lambda}$	spectral normal-hemispherical transmitted signal (%)
t	aging time (days)
T	temperature (°C or K)
T_c	temperature of the cold side silicon pad (°C)
T_m	temperature of the hot side silicon pad (°C)
$T_{d,\lambda}$	spectral diffuse transmittance (%)
$T_{nh,\lambda}$	spectral normal-hemispherical transmittance (%)
T_{vis}	visible transmittance (%)
V_p	cumulative pore volume (cm^3 g^{-1})
V_t	total pore volume (cm^3 g^{-1})
w	pore width (nm)
w_p	peak pore width (nm)
W^*, u^*, v^*	trichromatic coordinates

Greek symbols

θ	water contact angle (°)
λ	wavelength (nm)
ρ_s	density of bulk silica (g cm^{-3})
σ_{np}	standard deviation of nanoparticle size distribution (nm)
ϕ	porosity
ϕ_w	water volume fraction

1. Introduction

Silica aerogels are porous materials with large porosities (as high as 99.9%), large specific surface areas (100–1600 m^2 g^{-1}), low effective densities (as low as 0.003 g cm^{-3}), low thermal conductivities (on the order of 0.015 W m^{-1} K^{-1} at ambient conditions), low refractive indices (as low as 1.007), and low dielectric constants (as low as 1.1) [1–3]. The combination of these properties makes them useful (i) as optically-transparent thermal insulation in solar-thermal energy conversion systems [4–8] and in window solutions [9,10], (ii) as optical supports with ultralow refractive index [11], (iii) as transparent dye hosts in laser amplification [12], and (iv) as low-k dielectric materials in microelectronics [2].

Generally, silica aerogels are prepared by supercritical drying of silica gels synthesized via a sol-gel method [13]. Molecular precursors, such as tetramethyl orthosilicate (TMOS), tetraethyl orthosilicate (TEOS) and methyltriethoxysilane (MTES), are hydrolyzed in aqueous conditions to form reactive silica species that subsequently condense with each other to form a gel, i.e., a continuous silica network with pores filled with aqueous solution [13]. In the supercritical drying step, the liquid contained in the pores (also called "pore liquid") is exchanged with liquid CO_2 at high pressure (>74 bar). The temperature is then raised above the CO_2 critical temperature of 31 °C [14], which transforms liquid CO_2 into a supercritical fluid that can be slowly vented from the reactor

[13]. This process virtually eliminates any capillary forces imposed on the silica network by the pore liquid by replacing the liquid with supercritical CO_2, thus preventing shrinkage and cracking of the gel during drying [13]. On the other hand, silica xerogels are dried from water under ambient conditions. They feature porosities around 50% [15] and often crack [13] during drying due to the large capillary forces imposed on the soft silica network by the evaporating aqueous pore liquid. Although very effective at producing silica aerogel monoliths with large porosity, supercritical drying requires high-pressure equipment with limited sample space making the process expensive and difficult to scale up [15].

Freeze drying is an alternative drying method consisting of freezing the pore liquid before removing it by sublimation under reduced pressure [2]. The resulting porous materials, sometimes referred to as "cryogels" [2], have porosities and specific surface areas similar to those of aerogels [2]. However, the cooling and vacuum required during the process increase the synthesis cost and require specialized equipment compared with drying at ambient temperature and pressure [15]. Moreover, the crystals of frozen pore liquid formed during freezing leave large pores that scatter light and render the material hazy or opaque [2].

Historically, the term "aerogels" has been reserved for porous materials dried using supercritical techniques [2]. However, the development of new drying methods, such as freeze drying, extended the use of the term to all materials with porosities substantially larger than that of xerogels, regardless of the synthesis

methods [2]. In this work, we use the terms "aerogels" and "xerogels" to refer to mesoporous silica with porosity above and below 70%, respectively.

A successful synthesis of silica aerogels at ambient conditions, sometimes referred to as "ambigels", was achieved by modifying the gels with organic groups to exploit the "spring back" effect [15]. In this method, hydroxyl groups on the internal surface area of the gels are replaced with organic groups by reaction with chlorosilanes such as trimethylchlorosilane (TMCS) [15]. The modified gels initially shrink when the pore liquid evaporates but expand back to almost its original volume once completely dried, i.e., in the absence of capillary forces [15]. The latter expansion, i.e., the "spring back," is possible because, in the absence of surface hydroxyl groups, no new bonds are formed that can prevent the expansion after the shrinkage. By contrast, plain silica gels retain the size imposed by the shrinkage process as previously separated surface hydroxyl groups come in close proximity and form new bonds, making the gels stiffer and preventing expansion [13]. Unfortunately, while aerogels synthesized using the "spring back" effect can retain large porosity, they are often hazy or opaque due to the presence of large pores (>50 nm) that scatter visible light and render the monoliths hazy [16–22].

Recently, Butts et al. [23] developed a new synthesis method producing mesoporous organo-silica ambigel slabs with large visible transmittance, small haze, and low thermal conductivity. These slabs were synthesized by co-condensation of TEOS and MTES precursors, post-gelation surface modification with TMCS, and drying at ambient conditions. Ambient drying was preceded by exchange of the aqueous pore liquid with ethanol and heptane to reduce capillary forces in the gel during drying. The resulting slabs had thermal conductivity below 0.04 W m^{-1} K^{-1} while the visible transmittance of 1 mm thick monoliths exceeded 95% and the visible haze was below 5%. Such low thermal conductivity was achieved through the combination of large porosity (>80%) and large fractal dimension (>2.3). Indeed, such a large fractal dimension resulted in thermal conductivity comparable with that of silica aerogels with much larger porosity (ϕ > 90%). The high optical transparency was attributed to the small pore size and narrow pore size distribution that reduced volumetric light scattering. Other organosilica ambigels with high transparency (~80% at 550 nm and 2 mm thick) and low thermal conductivity ($\approx$0.015 W m^{-1} K^{-1} at ambient conditions) synthesized using ambient drying have been reported [24–26]. Despite the excellent thermal and optical performance of the monoliths produced by this method, the cost of organosilane might be prohibitive for some applications. In addition, the poor thermal stability of organosilica may limit the possible applications of these materials. In addition, this method may not be readily applicable to non-siliceous ambigels due to the lack of appropriate molecular precursors.

We recently reported a novel synthesis method producing transparent nanoparticle-based mesoporous silica monoliths using a template-free sol-gel synthesis on omniphobic liquid substrates at ambient conditions [27]. For the first time, omniphobic perfluorocarbon (PFC) liquids were used as substrates in a sol-gel synthesis of mesoporous materials (i) to reduce adhesion of the gels to the substrate and (ii) to provide an optically smooth liquid-liquid interface that produced surfaces with minimal roughness and surface light scattering [27]. The use of perfluorocarbon (PFC) liquid substrate also prevented cracking of a gel by reducing the stress imposed on the gels by the compressive and adhesive forces during the aging and drying stages [27]. In addition, the synthesis used small silica nanoparticles (6–12 nm in diameter) as building blocks of the monoliths to obtain small pores (<10 nm in width) between nanoparticles with a narrow size distribution [27]. The pores were much smaller than the wavelength of visible light (380–740 nm)

resulting in large normal-hemispherical transmittance and small haze for millimeter-thick slabs [27]. The slabs were made in the form of either disks or squares with rounded corners with diameters or edge lengths up to 4.5 cm, depending on the shape and size of the molds used [27]. However, the slabs were dried from water resulting in relatively low porosity (46–56%) and moderately low effective thermal conductivity (0.10–0.16 W m^{-1} K^{-1}) compared with much more porous albeit more hazy aerogels [27].

This paper presents a new method using colloidal silica nanoparticles as building blocks to synthesize silica aerogel slabs with high visible transmittance and low effective thermal conductivity at near ambient conditions. The use of nanoparticles as building blocks avoids the need for molecular precursors and prevents incorporation of easily degradable organic groups. It also offers a synthesis route that can be generalized to other material compositions. The study also aims to investigate the effects of the different synthesis parameters on the silica aerogels' microstructure as well as on their optical and thermal performance. The nanostructure of the synthesized aerogels was characterized by transmission electron microscopy (TEM), nitrogen porosimetry, and small-angle X-ray scattering (SAXS). Optical properties were characterized in terms of visible transmittance and haze while the thermal conductivity was measured using the guarded hot plate method. Hydrophobic aerogels were also prepared by a post-synthesis modification with an organochlorosilane and characterized by droplet contact angle measurements.

2. Experiments

2.1. Chemicals

Colloidal solutions of silica nanoparticles Nalco 2326 (15 wt% in water, NH$_4^+$ stabilized, lot number BP7J1239A1) were purchased from Nalco Chemical Company (Naperville, IL, USA). Hydrochloric acid (34–37% in water, TraceSELECT) was acquired from Sigma-Aldrich, Co. (St. Louis, MO, USA). Perfluoropolyether oils Krytox GPL 100, GPL 104, and GPL 106 with general formula [CF(CF$_3$)CF$_2$-O]$_n$ where n = 10–60 were procured from Miller-Stephenson Chemical Company Inc. (Danbury, CT, USA). Fluorinert FC-70 and perfluoro(tetradecahydrophenanthrene) (PFTDHP, 80%) were purchased from SynQuest Laboratories, Inc. (Alachua, FL, USA). Ethanol (200 proof), acetone (HPLC grade, 99.5%), and n-octane (97%) were acquired from Decon Labs, Inc. (King of Prussia, PA, USA), from Fisher Scientific (Fair Lawn, NJ, USA), and from Acros Organics (NJ, USA), respectively. Chlorotrimethylsilane (TMCS, 98+%) was acquired from Alfa Aesar (Haverhill, MA, USA). All chemicals were used as received without further purification.

2.2. Materials synthesis

Scheme 1 shows the synthesis method used to produce transparent nanoparticle-based silica aerogel monoliths with gelling and aging on omniphobic PFC liquid substrates followed by solvent exchange and drying under ambient conditions.

Optionally, the nanoparticle-based silica aerogel slabs can be made hydrophobic by post-synthesis reaction with TMCS vapor. Specifically, the as-synthesized slabs were placed in a sealed container holding TMCS vapor and left to react overnight. The transparent slabs became hazy after reacting with TMCS. However, the hazy appearance disappeared once the slabs were heated at 160 °C. Note also that no haze was observed if the slabs were degassed at 160 °C prior to the reaction with TMCS. This indicates that the haze was likely due to the reaction of TMCS with residual water physically adsorbed on the internal surface of the aerogels. Hydrophobic aerogels prepared in this manner are discussed
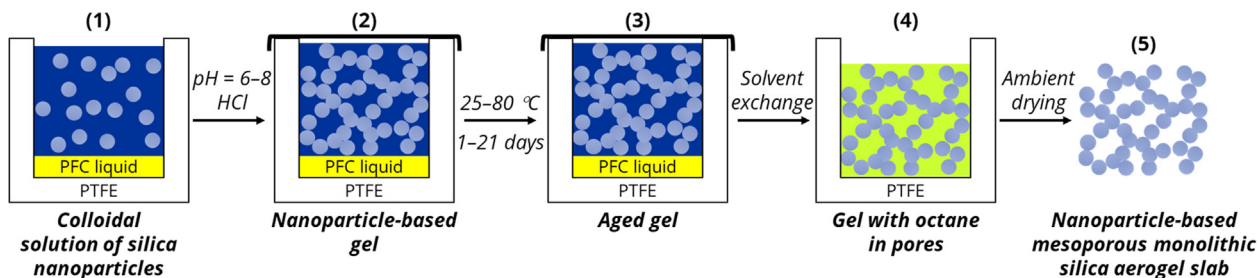
Scheme 1. The synthesis method used to produce transparent nanoparticle-based silica aerogel monoliths with gelling and aging on omniphobic PFC liquid substrates followed by solvent exchange and drying under ambient conditions.

exclusively in Section 3.5 while the rest of the manuscript discusses properties of the as-synthesized aerogel slabs.

Finally, this study used commercial colloidal silica nanoparticles, but any colloidal silica nanoparticles can be used in the proposed synthesis. Moreover, the same synthesis (Scheme 1) could potentially be used to synthesize aerogel slabs made of other nanoparticles such as titania and zirconia. Also, most PFC liquids were recovered after the synthesis and were reused in subsequent experiments. This was made possible by the omniphobic properties of the PFC liquids ensuring that they did not mix with the aqueous colloidal solution and could be easily recovered once the gels had formed. Indeed, the colloidal solution and the gels had densities below 1.6 g cm^{-3}, and, thus, floated on the PFC liquids whose densities were in the range 1.9–2.0 g cm^{-3} [28–30]. Finally, variants of the Krytox GPL oils with slightly different molecular weights, i.e., GPL 100, 104, and 106, were used interchangeably in the experiments and are collectively referred to as GPL PFC liquids since our previous study did not observe any differences between the materials synthesized on the different GPL liquids [27].

2.3. Characterization methods

Structural characterization. The average thickness L (in mm) of the nanoparticle-based silica aerogel slabs was calculated as a mean of the slab minimum and maximum thicknesses measured at different locations using a caliper. This was performed to accurately estimate the thickness of the slabs for the purpose of comparing their visible transmittance T_{vis} and haze h_{vis}.

Transmission electron microscope images of the nanoparticle-based silica aerogels were taken using a 200 kV FEI Tecnai TF20 TEM equipped with a field emission gun. The samples were ground, suspended in ethanol, sonicated for 3 min, applied onto a 400-mesh carbon-coated copper TEM grid, and dried in air before TEM analysis. The diameters d_{np} of at least 100 distinct silica nanoparticles were manually measured using ImageJ [31] software to calculate the average diameter $\bar{d}_{np}$ and standard deviation σ_{np} of the silica nanoparticles.

Low-temperature nitrogen adsorption–desorption isotherms were measured at –196 °C using a surface area and porosity analyzer TriStar II 3020 (Micromeritics Instrument Corp., Norcross, GA, USA). Most samples were degassed in vacuum at 160 °C with a few at 150–200 °C for 20–24 h prior to the measurements. The long degassing time ensures that all samples were sufficiently outgassed and that the narrow temperature range did not cause any structural change. The specific surface area S_{BET} (in m^2 g^{-1}) was calculated by applying the Brunauer–Emmett–Teller (BET) method [32] to the nitrogen adsorption data in the relative pressure range p/p_0 = 0.05–0.2 and assuming the nitrogen molecule cross-sectional area to be 0.162 nm^2 [33]. The total pore volume V_t (in cm^3 g^{-1}) was estimated based on the number of moles of nitrogen

adsorbed at relative pressure p/p_0 = 0.98 and assuming that the nitrogen in the pores was in the liquid state with molar density of 34.38 cm^3 mol^{-1} [34]. Then, the porosity ϕ of the nanoparticle-based silica aerogels was calculated as [35]

$$\phi = \frac{V_t \rho_s}{1 + V_t \rho_s}.$$ (1)

where ρ_s = 2.2 g cm^{-3} is the density of bulk silica [14].

The pore size distribution dV_p/dw was calculated using the Kruk–Jaroniec–Sayari method [36] based on the Barrett–Joyner–Halenda (BJH) method [37] and using (i) the adsorption branch of nitrogen isotherm, (ii) the modified Kelvin equation [36] calibrated for cylindrical pores up to 19 nm in diameter, and (iii) the statistical film thickness curve derived from the nitrogen adsorption isotherm measured for macroporous silica LiChrospher Si-1000 [38]. The peak pore width w_p (in nm) was estimated as the maximum of the pore size distribution, i.e., $d^2V_p/dw^2(w = w_p) = 0$.

The surface fractal dimension D_s was calculated based on nitrogen adsorption data according to [39]

$$\ln n = (D_s - 3)\ln A + B \ With \ A = RT\ln p/p_0$$ (2)

where n (in moles) is the measured amount of adsorbed nitrogen at relative pressure p/p_0, B is a fitting constant, R (=8.314 K mol^{-1} K^{-1}) is the universal gas constant [14], and T (=77.4 K) is the temperature during adsorption measurements.

Two-dimensional small-angle X-ray scattering (2D-SAXS) patterns were collected at the Stanford Synchrotron Radiation Lightsource using beam line 1–5, with a wavelength of 0.1033 nm operating at an X-ray energy of 12.002 keV. A sample-to-detector distance of 2.870 m was used in conjunction with a Rayonix-165 CCD detector. The 2D-SAXS data was calibrated using silver behenate, and then reduced using the Nika package from Igor Pro [40]. The reduced SAXS patterns were then fitted using the Unified fit macro in the Irena package [41] by applying two Guinier-Porod levels [42–44] for magnitude of the scattering vector q in the range q = 0.03–0.1 Å^{-1} (Level 1) and q = 0.01–0.03 Å^{-1} (Level 2). The R_g-cutoff parameter was applied for the second level to treat both levels as representing one population of scatterers. The fitting resulted in two sets of parameters describing each of the Guinier-Porod levels, namely a Porod exponent P_1 and radius of gyration R_{g1} for Level 1 and a Porod exponent P_2 and radius of gyration R_{g2} for Level 2 (see Table S1 in Supplementary material). The diameters of the associated X-ray scatterers d_1 and d_2 were calculated assuming a dense-sphere shape according to

$$d_1 = 2\sqrt{\frac{5}{3}}R_{g1} \ and \ d_2 = 2\sqrt{\frac{5}{3}}R_{g2}$$ (3)

Optical characterization. The spectral normal-hemispherical transmitted signal $S_{nh,\lambda}$ and diffuse transmitted signal $S_{d,\lambda}$ through the nanoparticle-based silica aerogel monoliths were measured

with a double-beam UV–Vis spectrometer 3101-PC (Shimadzu, Kyoto, Japan) equipped with an integrating sphere ISR 3100 (Shimadzu, Kyoto, Japan) with internal diameter of 6 cm. Then, the spectral normal-hemispherical transmittance $T_{nh,\lambda}$ was calculated as

$$T_{nh,\lambda} = \frac{S_{nh,\lambda} - D_{nh,\lambda}}{B_{nh,\lambda} - D_{nh,\lambda}} \tag{4}$$

where $D_{nh,\lambda}$ is the dark signal collected in the absence of light and $B_{nh,\lambda}$ is the reference signal measured in the absence of a sample using the same procedure as that used to measure $S_{nh,\lambda}$. In addition, the spectral haze h_λ was calculated according to ASTM D1003-13 standard as [45]

$$h_\lambda = \frac{S_{d,\lambda}}{S_{nh,\lambda}} - \frac{M_{d,\lambda}}{B_{nh,\lambda}} \tag{5}$$

where $M_{d,\lambda}$ was the signal measured in the absence of a sample using the same procedure as that used to measure $S_{d,\lambda}$. Then, the visible transmittance T_{vis} and haze h_{vis} of nanoparticle-based silica aerogel monoliths were calculated as [46,47]

$$T_{vis} = \frac{\int_{380}^{780} P_\lambda T_\lambda d\lambda}{\int_{380}^{780} P_\lambda d\lambda} \ and \ h_{vis} = \frac{\int_{380}^{780} P_\lambda h_\lambda d\lambda}{\int_{380}^{780} P_\lambda d\lambda} \tag{6}$$

where P_λ is the photopic spectral luminous efficiency function of the human eye [46], i.e., the function representing the wavelength-dependent sensitivity of the eye during daytime.

The color rendering index *CRI* ranges from 0 to 100 and quantifies the quality of reproduction of colors transmitted through transparent and semitransparent materials. The *CRI* of the synthesized nanoparticle-based silica aerogel monoliths was calculated according to BS EN 410:2011 standard [48] and taking the CIE (International Commission on Illumination) illuminant D_{65} as the light source. The *CRI* is expressed as [48]

$$CRI = \frac{1}{8} \sum_{i=1}^{8} (100 - 4.6\Delta E_i) \tag{7}$$

where ΔE_i is the geometrical distance between the perceived color with and without a sample for the ith test color. The geometrical distance ΔE_i was calculated for each of the eight test colors considered as [48]

$$\Delta E_i = \sqrt{\Delta W_i^{*2} + \Delta u_i^{*2} + \Delta v_i^{*2}} \ with \ i = 1, 2, \cdots, 8 \tag{8}$$

where ΔW_i^*, Δu_i^*, and Δv_i^* are distances, in the CIE 1964 uniform color space domain, between the trichromatic coordinates perceived with and without a sample for the ith test color. The trichromatic coordinates W_i^*, u_i^*, and v_i^* of each test color perceived with a sample were calculated from the spectral normal-hemispherical transmittance $T_{nh,\lambda}$ while those perceived without a sample, i.e., of the reference illuminant D_{65}, were taken from BS EN 410:2011 standard [48]. A *CRI* above 95 and close to 100 represents good and excellent color reproduction, respectively [49]. As a reference, most glass and windows have *CRI* in the range 80–96 [50].

FTIR characterization. Pellets for the FTIR measurements were prepared by grinding 7 mg of the nanoparticle-based mesoporous slab with 150 mg of potassium bromide (KBr) using a mortar and pestle until a fine powder was obtained. Then, 15 mg of the powder mixture was pressed into a pellet using a pellet press (Mini-Pellet Press Kit – Asia, Specac, UK) under 1.5 ton load. The spectral normal-normal transmittance of the pellets was measured using a nitrogen-purged FTIR spectrometer (Nicolet™ iS50, Thermo Sci-

entific Fischer, USA). A potassium bromide (KBr) beamsplitter with a deuterated triglycine sulfate (DTGS) detector was used in the 2.5–20 μm spectral range.

Thermal conductivity characterization. The effective thermal conductivity k_{eff} of the nanoparticle-based silica aerogel slabs was measured at room temperature using a guarded hot plate apparatus similar to that described in Ref. [51] following the C177-13 ASTM standard [52] and operated in a single-sided mode. Specifically, an aerogel monolith was placed between two 1 mm thick 3 M silicone thermal pads no. 5519 (3 M, Saint Paul, MN, USA) with thermocouples embedded in each pad. Then, the padded sample was sandwiched between a cold plate and a hot plate. Finally, the entire stack was placed between two blocks of expanded polystyrene and gently compressed to ensure good thermal contact. The ensemble was wrapped in multiple layers of insulation cloth to minimize heat loss. The temperature of the cold plate was controlled by a chiller circulating water at constant temperature T_c. The hot plate consisted of two concentric sections, each with a separate set of resistive wires that were connected to two separate power supplies to independently control currents and, thus, the heat generated in each section by Joule heating. The inner section was used for thermal conductivity measurement while the outer section was used to minimize lateral heat losses. The effective thermal conductivity was calculated under steady state conditions based on energy conservation principles and Fourier's law according to

$$k_{eff} = \frac{\dot{Q}_m L}{A_m(T_m - T_c)} = \frac{R_m I_m^2 L}{A_m(T_m - T_c)} \tag{9}$$

Here, $\dot{Q}_m$ is the heat generation rate (in W) at steady state ($\dot{Q}_m = R_m I_m^2$) where R_m is the resistance (in Ω) of the resistive wires embedded in the hot plate inner section, I_m is the supplied current (in A), A_m is the area of the inner section (in m²), and T_c and T_m are the temperatures (in °C) recorded by thermocouples embedded in silicon pads on the cold and hot sides of the sample, respectively. Note that T_c and T_m were controlled to ensure that the average temperature of the measurement was at room temperature and that $T_m - T_c$ was large enough (~10 °C) to achieve acceptable experimental uncertainties per ASTM standard.

Contact angle measurements. The water droplet contact angle θ on the hydrophobic nanoparticle-based silica aerogels was measured by the static sessile drop method using a FTÅ125 contact angle goniometer (First Ten Ångstroms Inc., Portsmouth, VA, USA). Before any measurement, the surface of the slabs was cleaned from any dust by flowing nitrogen gas. Then, a water droplet, with volume of 0.02 to 0.10 mL, was placed onto the slab's surface. The contact angle was determined by non-spherical liquid-vapor curve fitting using the Fta32 Video 2.1 software (First Ten Ångstroms Inc). Measurements were performed multiple times on the top and bottom sides of the slab with droplets of different sizes and at various locations. The reported contact angle and the associated uncertainty were calculated as the mean and standard deviation of the mean value of all measurements, respectively.

3. Results and discussion

3.1. Synthesis

The synthesis method (Scheme 1) developed in this study combined several strategies to synthesize large and thick silica aerogel monoliths with large visible transmittance and low thermal conductivity. First, the synthesis employed omniphobic substrates such as PTFE and PFC liquids to limit adhesion between the gel and the substrate. Our previous study [27] showed that non-stick substrates such as smooth PTFE and PFC liquids enable gels to

shrink freely during aging and drying without cracking because they lessened the competing stresses created by compressive capillary forces and adhesive forces. Note that PFC liquids are excellent substrates here because (i) they do not mix with the colloidal solution of silica nanoparticles, (ii) they have high density, ensuring that the colloidal solution floats on top of the PFC liquid, and (iii) they feature large surface tension with water, resulting in a flat and stable liquid-liquid interface between the colloidal solution and the PFC liquid. The latter interface produces aerogel slabs with an optically-smooth bottom surfaces that achieve high transmittance and low haze by reducing surface light scattering [27].

The second key strategy used here is the fact that the aerogels were synthesized using small silica nanoparticles (d_{np} = 6–12 nm) as building blocks, so as to reduce visible light scattering and to achieve high visible transmittance and low haze. Scattering was limited because the silica nanoparticles and the mesopores separating them were much smaller than the wavelength of light. The use of nanoparticles also helped avoid excessive shrinkage during aging, resulting in large porosity and reduced risks of cracking. The shrinkage was limited because almost all silica was bound in the silica nanoparticles and only a small amount of reactive silica was available in the solution; reactive silica can cause the gel to shrink through condensation reactions [13].

The third key processing step was to gel the colloidal solution of the nanoparticles by lowering the pH. This method produced gels with a large volume fraction of water, resulting in aerogels with larger porosity compared with our previous approach of gelation by evaporation [27]. It is also significantly faster than evaporative gel formation, with gels forming in a few minutes to hours, as opposed to several days. Note that the stability of any colloidal solution depends on the size, concentration, and surface charge of the suspended nanoparticles [13]. Lowering the pH reduced the surface charge of the nanoparticles, destabilizing the colloidal solution and leading to gelation. The nanoparticle-based gels contained the same water volume fraction ($\phi_w \approx 93$ vol%) as the original colloidal solution since no water was removed during the process.

Fourth, to reduce shrinkage and prevent cracking, the gel slabs were aged at temperature above 25 °C to improve their mechanical strength before drying. During aging, Ostwald ripening results in dissolution of silica from regions of the gel with high curvature and precipitation in regions of low curvature resulting in silica transport (i) from small to large nanoparticles and (ii) from nanoparticles to the necks connecting them [13]. This process is slow at room temperature but is greatly accelerated at elevated temperatures due to the combined increase of (a) kinetics of dissolution and precipitation, (b) solubility, and (c) diffusion coefficient of silica in water [13].

Finally, in the fifth key processing strategy, the aged gel slabs were dried ambiently by exchanging water contained in the pores of the gels with octane [53]. This exchange reduced the capillary forces during drying because the surface tension of the octane/air interface is three times smaller than that of the water/air interface (i.e., 21.17 vs. 72.06 mN m^{-1}) [14]. Here, octane was preferred over other solvents with similar surface tension such as cyclohexane and heptane [53] because it has a much lower vapor pressure of 1.86 kPa at 25 °C compared with 13.0 and 6.09 kPa for cyclohexane and heptane, respectively [14]. This greatly reduced the evaporation rate and the occurrence of cracking [14].

Table 1 summarizes the conditions and structural characterization of the nanoparticle-based silica aerogels synthesized in the present study. Note that results for the nanoparticle-based mesoporous silica slabs reported in Ref. [27] are also included as a reference.

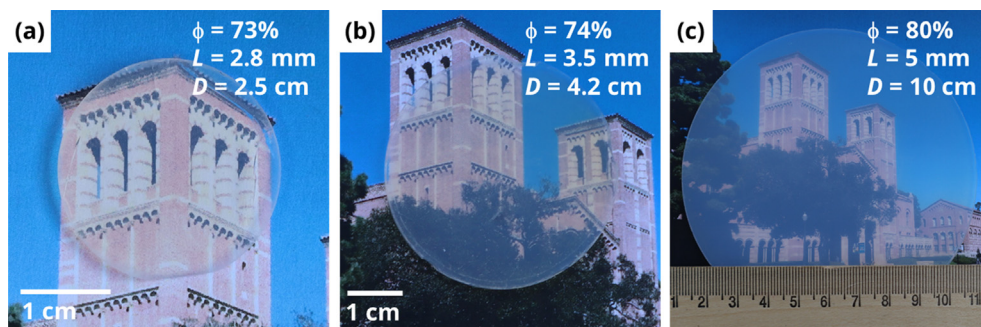## 3.2. Optical characterization

Fig. 1 shows photographs of transparent nanoparticle-based silica aerogel monoliths synthesized on omniphobic substrates (Scheme 1) and aged using different conditions, namely (a) Sample 3 synthesized on PTFE and aged at room temperature for 1 day, (b) Sample 7 synthesized on PTFE and aged at 40 °C for 3 days, and (c) Sample 21 synthesized on PFC liquid and aged at 50 °C for 14 days. Note that all the monoliths shown were dried from octane and calcined in oxygen at 450 °C for 4 h. Fig. 1 shows that the aerogel slabs were circular and optically transparent with a slight blue tint. Their porosity ϕ was between 73% and 80%, their diameter D ranged from 2.5 to 10 cm, and their thickness L was between 2.8 and 5 mm. The diameter D was controlled by the diameter of the mold used, which ranged from 3.8 to 14.2 cm. Their thickness was determined by the initial volume of the colloidal solution. Note that it is also possible to use molds of different shapes, such as a square, as demonstrated previously [27].

Fig. 2(a) shows the spectral normal-hemispherical transmittance $T_{nh,\lambda}$ for the three representative aerogel slabs shown in Fig. 1. It indicates that the transmittance $T_{nh,\lambda}$ increased with increasing wavelength from 400 to 700 nm due to stronger scattering at wavelength $\lambda < 500$ nm resulting in the blue tint observed in Fig. 1. This was confirmed by the spectral haze h_λ (Fig. S1 in Supplementary material). Moreover, Fig. 2(a) compares the transmittance $T_{nh,\lambda}$ of Samples 3, 7, and 11 with that of a precursor-based supercritically-dried silica aerogel slab of thickness L = 5.5 mm and porosity ϕ = 96% reported by Zhao et al. [54]. Similarly, Fig. 2(b) compares the transmittance $T_{nh,500}$ at wavelength λ = 500 nm for Samples 3, 7, and 11 with that of the precursor-based silica aerogels reported in Ref. [54] as a function of thickness. Both figures indicate that the present aerogels with porosity of 70–80% had much higher normal-hemispherical transmittance than conventional aerogels. This was likely due to the presence of larger pores with larger porosity in supercritically dried aerogels resulting in stronger light scattering and, thus, smaller transmittance and larger haze. Thus, slightly less porous nanoparticle-based aerogels with considerably larger transmittance may be more appropriate than conventional aerogels for applications where optical transparency is essential, such as for window solutions and solar-thermal conversion systems.

Table 2 summarizes the optical characterization of Samples 3, 7, and 11 considered in Figs. 1 and 2. It shows that the visible transmittance T_{vis} decreased with increasing thickness L but still exceeded 75% even for slabs as thick as 5.0 mm. Table 2 also indicates that these aerogel slabs featured a color rendering index (*CRI*) exceeding 90 indicating relatively good color reproduction.

3.3. Structural characterization

3.3.1. TEM characterization

Fig. 3 shows (a,c) TEM images and (b,d) particle size histogram (blue) and Gaussian distribution fit (red) of the nanoparticle-based silica aerogels synthesized on omniphobic substrates and aged using different conditions, namely (a,b) Sample 4 aged at room temperature for 1 day and (b,d) Sample 25 aged at 80 °C for 1 day. Note that both aerogels were synthesized on PTFE, dried from octane, and analyzed without calcination. Figs. 3(a) and 3 (b) indicate that Sample 4 was made of loosely aggregated silica nanoparticles with diameter d_{np} = 5.9–8.9 nm and little to no necks between them. By contrast, Figs. 3(c) and 3(d) show that Sample 25 was made of silica nanoparticles of diameter d_{np} = 7.1–11.9 nm connected with thick necks such that the larger the nanoparticle diameter, the thicker the necks. In addition, the wide particle size

Table 1
Summary of the synthesis conditions and structural characterization of the nanoparticle-based silica aerogels synthesized in the present study. Results for nanoparticle-based mesoporous silica slabs reported in Ref. [27] are also included as a reference.

Sample	Substrate	Aging temp./time	Drying solvent	Calcination	S_{BET} (m^2/g)	V_t (cm^3 g^{-1})	ϕ (%)	w_p (nm)
SiO$_2$-PTFE-rt [27]	PTFE	25 °C/>3 days	Water	–	390	0.42	48	6.1
SiO$_2$-PFC-rt [27]	PFC (GPL)	25 °C/>3 days	Water	450 °C/2h	400	0.38	46	5.0
SiO$_2$-PTFE-hc [27]	PTFE	25 °C/>3 days	Water	–	390	0.41	47	5.5
SiO$_2$-PFC-hc [27]	PFC (GPL)	25 °C/>3 days	Water	450 °C/2h	360	0.44	49	5.8
SiO$_2$-PTFE-40C [27]	PTFE	40 °C/>3 days	Water	–	380	0.57	56	7.6
SiO$_2$-PFC-40C [27]	PFC (GPL)	40 °C/>3 days	Water	450 °C/2h	370	0.53	54	7.2
1	PTFE	50 °C/1 day	Water	–	380	0.57	56	8.0
2	PTFE	25 °C/1 day	Octane	–	390	1.21	73	17.2
3	PTFE	25 °C/1 day	Octane	450 °C/4h	390	1.18	72	18.3
4	PTFE	25 °C/1 day	Octane	–	360	1.13	71	16.8
5	PTFE	25 °C/1 day	Octane	–	390	1.22	73	17.6
6	PTFE	25 °C/21 days	Octane	–	400	1.04	70	13.5
7	PTFE	40 °C/3 days	Octane	450 °C/4h	370	1.31	74	17.7
8	PTFE	50 °C/1 day	Octane	–	380	1.32	74	18.2
9	PTFE	50 °C/2 days	Octane	–	370	1.67	79	21.1
10	PTFE	50 °C/3 days	Octane	–	300	1.49	77	21.8
11	PTFE	50 °C/3 days	Octane	450 °C/4h	370	1.57	78	22.6
12	PFC (GPL)	50 °C/4 days	Octane	–	360	1.67	79	21.5
13	PFC (FC-70)	50 °C/4 days	Octane	–	350	1.50	77	19.4
14	PFC (PFTDHP)	50 °C/4 days	Octane	–	420	1.55	77	24.9
15	PFC (PFTDHP)	50 °C/5 days	Octane	–	350	1.65	78	22.6
16	PTFE	50 °C/6 days	Octane	–	340	1.68	79	24.2
17	PFC (GPL)	50 °C/6 days	Octane	–	340	1.78	80	26.0
18	PFC (FC-70)	50 °C/6 days	Octane	–	390	1.71	79	24.0
19	PFC (PFTDHP)	50 °C/6 days	Octane	–	350	1.55	77	25.9
20	PFC (GPL)	50 °C/7 days	Octane	–	340	1.86	80	24.7
21	PFC (FC-70)	50 °C/14 days	Octane	450 °C/4h	340	1.84	80	25.0
22	PTFE	60 °C/1 day	Octane	–	350	1.36	75	20.3
23	PTFE	60 °C/1 day	Octane	–	370	1.43	76	19.6
24	PTFE	60 °C/1 day	Octane	–	360	1.36	75	19.0
25	PTFE	80 °C/1 day	Octane	–	360	1.91	81	26.0

Fig. 1. Photographs of transparent nanoparticle-based silica aerogel monoliths synthesized on omniphobic substrates and aged using different conditions (Scheme 1) namely (a) Sample 3 synthesized on PTFE and aged at room temperature for 1 day, (b) Sample 7 synthesized on PTFE and aged at 40 °C for 3 days, and (c) Sample 21 synthesized on PFC and aged at 50 °C for 14 days (Table 1). All three slabs were dried from octane and calcined in oxygen at 450 °C for 4 h. The slab porosity ϕ, thickness L, and diameter D are indicated in each panel.

distribution observed in Sample 25 was typical of Ostwald ripening caused by aging of the gel at 80 °C [13]. Fig. 3 also establishes that both Samples 4 and 25 had interconnected mesopores within a network of silica nanoparticles. While the pores size cannot be fully determined from the images (instead, see next section on porosimetry), the pores do appear to be larger in Sample 25 than in Sample 4, indicating that the pore size tends to be comparable to that of the nanoparticles. This same conclusion has been drawn previously using computer simulations of mesoporous materials made of nanoparticles of different sizes [55]. Overall, the TEM images provide direct evidence of colloid growth during aging at elevated temperature and suggest that the lowest possible aging temperatures that produce mechanical robustness should be used to improve optical clarity.

3.3.2. Nitrogen porosimetry

Fig. 4 shows (a) nitrogen adsorption–desorption isotherms and (b) the corresponding adsorption pore size distributions (PSDs) dV_p/dw of the nanoparticle-based silica aerogels synthesized in PTFE molds and aged for 1 day at temperatures T of 25 to 80 °C followed by solvent exchange. These four samples were selected to discuss the general features and structure of pores common to all aerogels considered in this study. Note that nitrogen adsorption–desorption isotherms and the corresponding pore size distributions of all other aerogels are included in the Supplementary material (Figs. S2 and S3). All isotherms were of type IV(a) with H2(b) hysteresis loops, according to the IUPAC classification [56,57], indicating that the aerogel pore structures consisted of interconnected mesopores with different sizes [56,57]. This observation is
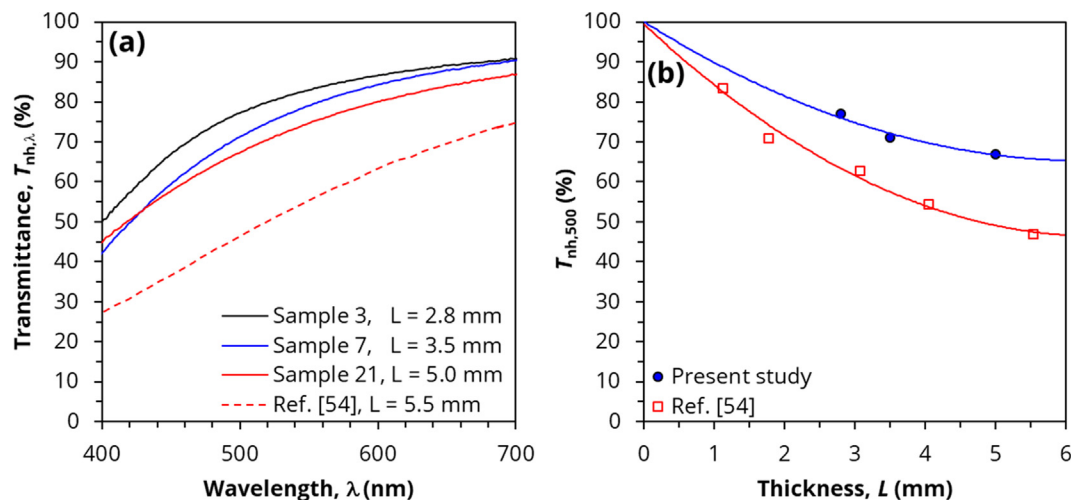
Fig. 2. (a) Spectral normal-hemispherical transmittance $T_{nh,\lambda}$ of the transparent nanoparticle-based silica aerogel monoliths shows in Fig. 1 and of a precursor-based silica aerogel slab with thickness L = 5.5 mm and porosity ϕ = 96% reported in Ref. [54] and (b) normal-hemispherical transmittance $T_{nh,500}$ of the same three nanoparticle-based aerogel slabs and of precursor-based silica aerogels reported in Ref. [54] as a function of thickness. Note that lines serve as eye guides only.

Table 2
Optical characterization of selected transparent nanoparticle-based silica aerogel monoliths synthesized on omniphobic substrates and aged using different conditions (see Table 1).

Sample	Porosity, ϕ (%)	Peak pore width, w_p (nm)	Thickness, L (mm)	Visible transmittance, T_{vis} (%)	Visible haze, h_{vis} (%)	CRI
3	72	18.3	2.8	83	20	93
7	74	17.7	3.5	79	17	91
21	80	25.0	5.0	75	31	91

consistent with the mesoporous structure observed in TEM images (Fig. 3). Fig. 4(b) shows that the aerogels had broad pore size distributions with pore width ranging from $w \approx$ 5–7 nm up to $w \approx$ 26–35 nm. Notably, Fig. 4 shows that increasing the aging temperature from T = 25 to 80 °C increased the porosity and the peak pore width w_p, and broadened the pore size distribution, as explained later in the section "Effects of aging temperature and duration".

We next consider how key parameters, including the specific surface area, the fractal dimension, and the average pores size, change with the overall porosity. Fig. 5 shows (a) the specific surface area S_{BET} and the surface fractal dimension D_s and (b) the peak pore width w_p as functions of porosity ϕ for the synthesized nanoparticle-based silica aerogels (Table 1) and for the mesoporous slabs reported previously [27]. Fig. 5(a) indicates that their specific surface area S_{BET} did not significantly depend on either the porosity ϕ or the aging conditions. In addition, comparing mesoporous slabs [27] aged at room temperature and dried from water (SiO_2-PTFE-rt, SiO_2-PFC-rt, SiO_2-PTFE-hc, SiO_2-PFC-hc) with aerogels also aged at room temperature but dried from octane (Samples 2–5) established that the specific surface area S_{BET} was also unaffected by the drying solvent. Fig. 5(a) further indicates that the surface fractal dimension D_s of the nanoparticle-based silica aerogels and mesoporous slabs [27] synthesized on omniphobic substrates exceeded 2.5 and increased almost linearly with increasing porosity ϕ.

Fig. 5(b) establishes that the peak pore width w_p increased sharply with increasing porosity ϕ namely from 5 nm to 25 nm as porosity increased from 50% to 80%. This observation can be attributed to the fact that the solvent-exchanged gel slabs were subjected to less compression during drying thanks (i) to lower capillary forces from octane evaporation and/or (ii) to a stronger and stiffer structure obtained from aging above room temperature. Fig. 5 also shows the theoretical predictions of the peak pore width for non-intersecting monodisperse cylindrical or spherical pores denoted by $w_{p,c}$ or $w_{p,s}$, respectively, and expressed as [35]

$$w_{p,c} = \frac{4V_t}{S_{BET}} = \frac{4\phi}{\overline{S_{BET}}\rho_s(1-\phi)} \quad and \quad w_{p,s} = \frac{6V_t}{\overline{S_{BET}}}$$

$$= \frac{6\phi}{\overline{S_{BET}}\rho_s(1-\phi)} \tag{10}$$

where $\overline{S_{BET}}$ = 368 m^2 g^{-1} is the specific surface area averaged over all samples listed in Table 1. Due to the complex shape of pores created between aggregated nanoparticles (Fig. 3), the peak pore width w_p measured from the pore size distribution of the aerogels [Fig. 4(b)] fell between $w_{p,c}$ and $w_{p,s}$.

3.3.3. Effects of solvent exchange

Table 1 indicates that using octane for ambient drying substantially increased the porosity of the aerogel samples compared with water [27], even without aging at elevated temperature. Specifically, all aerogel samples aged at room temperature and dried from octane (Samples 2–5) featured porosity ϕ = 71–73% and peak pore width w_p = 16.8–18.3 nm compared with ϕ = 46–49% and w_p = 5.0–6.1 nm for those synthesized at room temperature and dried from water (SiO_2-PTFE-rt, SiO_2-PFC-rt, SiO_2-PTFE-hc, SiO_2-PFC-hc) [27]. The increase in porosity with octane was due to the reduction in the capillary forces and in the compression of the nanoparticle network during drying.

Finally, the IR transmittance spectra (Fig. S5 in the Supplementary material) of KBr pellets of nanoparticle-based mesoporous silica samples dried from water (Sample 1) and octane (Sample 8) featured only peaks corresponding to Si—O—Si, Si—OH, and H_2O vibrational modes and none corresponding to C—H modes. Thus, all samples were composed of silica with no trace of organic substance observed.
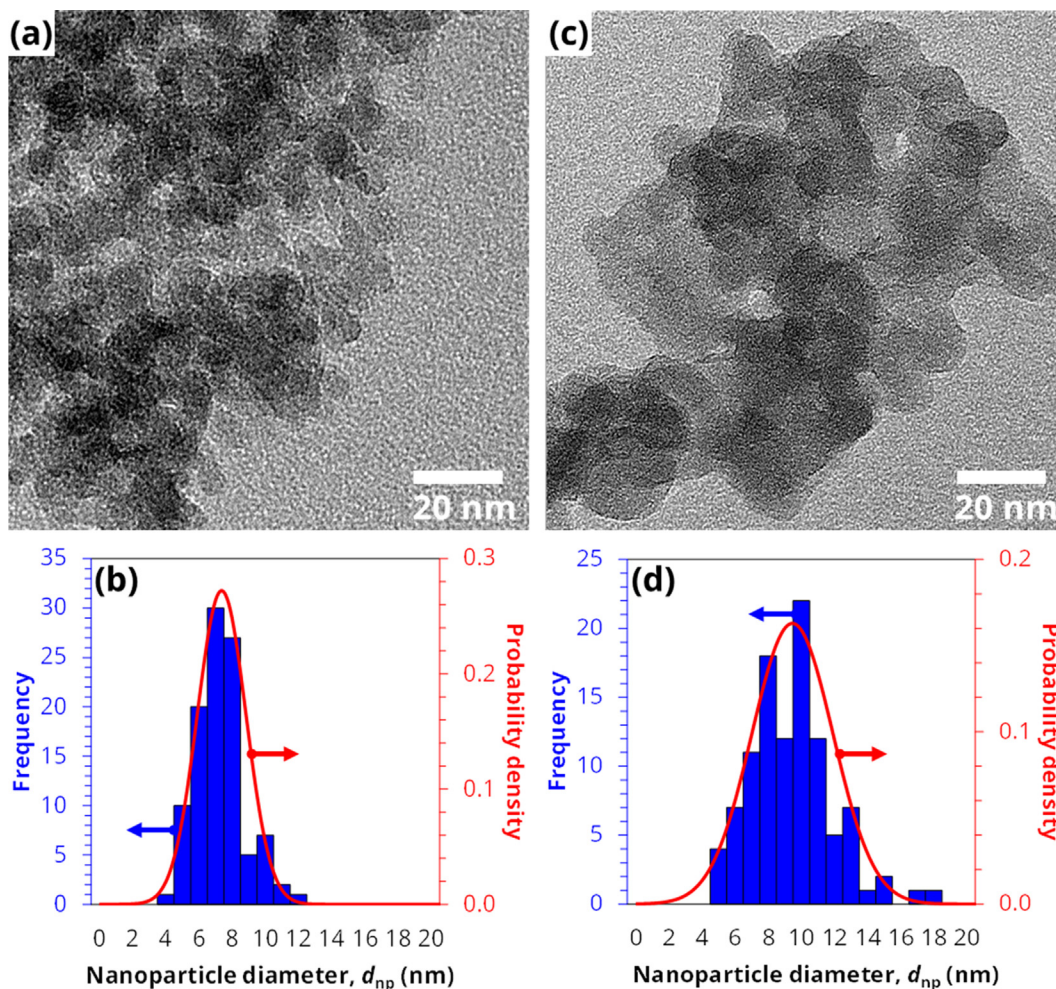
Fig. 3. (a,c) TEM images and (b,d) particle size histogram (blue) and Gaussian distribution fit (red) of the nanoparticle-based silica aerogels synthesized on omniphobic substrates and aged using different conditions namely (a,b) Sample 4 aged at room temperature for 1 day and (c,d) Sample 25 aged at 80 °C for 1 day. Note that both aerogels were synthesized on PTFE, dried from octane, and analyzed without calcination. (For interpretation of the references to color in this figure legend, the reader is referred to the web version of this article.)
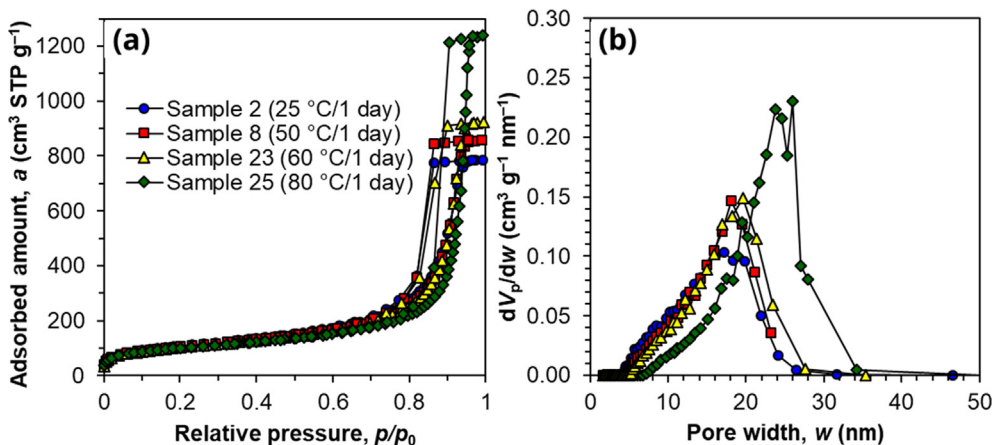
Fig. 4. (a) Nitrogen adsorption–desorption isotherms and (b) the corresponding adsorption pore size distributions of the nanoparticle-based silica aerogels synthesized on omniphobic substrates and aged at temperatures T = 25–80 °C.

3.3.4. Effects of aging temperature and duration

Fig. 6 shows the porosity ϕ and peak pore width w_p of the nanoparticle-based silica aerogels synthesized on omniphobic substrates as functions of (a) aging temperature T for aerogels aged for

1 day and (b) aging time t for aerogels aged at 50 °C (see Table 1). Fig. 6(a) indicates that the porosity ϕ increased from 72% to 81% and the peak pore width w_p increased from 17 nm to 26 nm as the aging temperature increased from 25 to 80 °C. The larger
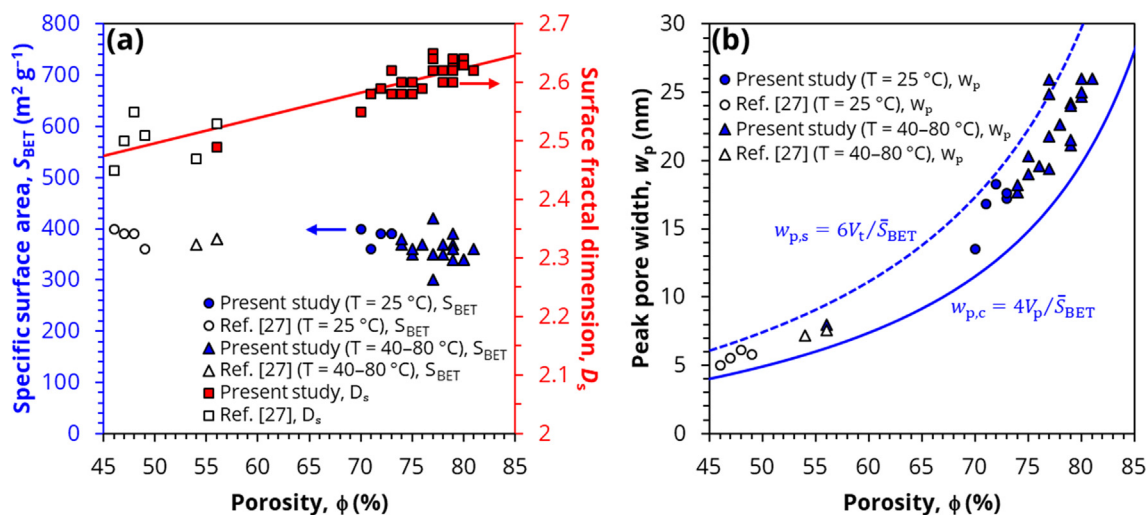
Fig. 5. (a) Specific surface area S_{BET} and surface fractal dimension D_s and (b) peak pore width w_p as functions of porosity ϕ for the present silica aerogels (Table 1) and for the mesoporous slabs synthesized in Ref. [27]. In panel (a): the red dashed line is a straight line fit of D_s vs. ϕ. In panel (b): the blue dotted and dashed lines represent the peak pore widths $w_{p,c}$ and $w_{p,s}$ calculated from Eq. (10) with $\bar{S}_{BET}$ = 368 m² g⁻¹, i.e., the average of all samples listed in Table 1. (For interpretation of the references to color in this figure legend, the reader is referred to the web version of this article.)

Fig. 6. Porosity ϕ and peak pore width w_p of the nanoparticle-based silica aerogel monoliths synthesized on omniphobic substrates (Table 1) as functions of (a) aging temperature T for aerogels aged for 1 day and (b) aging time t for aerogels aged at 50 °C. Note that all samples were dried from octane. The dotted and dashed lines are meant only to guide the eyes.

porosity and pore width and the wider pore size distribution (Fig. 4) resulted from a combination of larger colloidal building blocks (see Fig. 3) and a stronger, less compressible silica network obtained upon aging at higher temperature. For the same reasons, Fig. 6(b) establishes that the porosity increased from ϕ = 74% to 80% and peak pore width from w_p = 18.2 to 25 nm as the aging time t increased from 1 to 14 days at an aging temperature of 50 °C.

These results demonstrate that porosity can be increased by aging the gel at higher temperature and/or for a longer period of time. For example, Samples 21 and 25 both had porosity $\phi \approx$ 80% with Sample 21 aged at 50 °C for 14 days and Sample 25 aged at 80 °C for only 1 day. Note, however, that the aging temperature seems to have a much stronger impact on porosity and peak pore width than the aging duration. It is also worth noting that aging at higher temperature offers the benefit of reducing the synthesis duration and increasing productivity.

3.3.5. No effect of different omniphobic substrates or calcination on porosity

Table 1 indicates that (i) using different omniphobic substrates or (ii) calcining the dried slabs at 450 °C for 4 h had little to no effect on the porosity or peak pore width of the aerogels. For example, Samples 16–19 aged at 50 °C for 6 days had similar porosity ϕ = 77–80% and peak pore width w_p = 24.0–26.0 nm even though they were synthesized on different omniphobic substrates, namely PTFE, GPL PFC, FC-70 PFC, or PFTDHP PFC. Similarly, Samples 2 and 3 had similar porosity ϕ = 73 and 72% and peak pore width w_p = 17.2 and 18.3 nm without and with calcination, respectively. This result is important, because the ability to change omniphobic substrate and to forgo energy intensive calcination provides opportunities to optimize materials and processing for a variety of applications.

3.3.6. Small-angle X-ray scattering

Fig. 7(a) shows small-angle X-ray scattering patterns obtained on Samples 3, 7 and 25. These samples were chosen to be representative of all nanoparticle-based silica aerogels synthesized in the present study. All SAXS patterns consisted of two separate Guinier-Porod levels (i = 1,2), each characterized by its own Porod exponent P_i and radius of gyration R_{gi} (see Table S1). For all samples (Table S1), Level 1 featured a Porod exponent P_1 = 4, corresponding to non-fractal scatterers, i.e., dense particles with smooth surface. Similarly, for all samples, the Level 1 radius of gyration R_{g1} = 3–4 nm, corresponding to the radius of the silica nanoparticles, based on Eq. (3), and as observed in TEM images (Fig. 3). This indicates that Level 1 simply corresponded to silica nanoparticles used as building blocks of the mesoporous slabs. Level 2 featured a Porod exponent P_2 in the range 1.05–1.43 and radius of gyration R_{g2} in the range 5.6–10.3 nm, across all samples (see Table S1). This indicates that Level 2 was associated with the fractal structure ($P_2 = D_m$) of the pores created by the aggregated silica nanoparticles. In fact, Fig. 7(b) shows the diameter d_2 of the Level 2 scatterers, calculated by approximating the pores as solid spheres [Eq. (3)], correlates with the peak pore width w_p calculated from nitrogen porosimetry measurements. Fig. 7(b) indicates that the solid sphere approximation generally overestimated the pore size, on average by 10%. Finally, The size of the Level 2 scatterers d_2 increased with aging temperature T and duration t [Fig. 7(c, d)]. Interestingly, no correlation was observed between the Level 1 radius of gyration R_{g1} or the mass fractal dimension D_m (see Table 1) and the specific surface area, porosity, peak pore width, the substrate type, or the calcination conditions of the aerogels synthesized.

3.4. Thermal conductivity

Fig. 8 plots the effective thermal conductivity k_{eff} as a function of porosity ϕ for the nanoparticle-based silica aerogel slabs synthesized in the present study. For comparison, Fig. 8 also shows the effective thermal conductivity of other mesoporous silica materials with a wide range of porosities and different synthesis methods including (i) nanoparticle-based mesoporous silica slabs [27], (ii) nanoparticle-based mesoporous silica thin films [58], (iii) hydrophobic TEOS-based silica aerogels dried at ambient pressure [23,59,60], (iv) hydrophobic sodium silicate-based silica aerogels dried at ambient pressure [61], and (v) hydrophobic and hydrophilic silica aerogels dried using supercritical CO_2 [62]. The aerogel monoliths reported in the present study and the mesoporous silica slabs [27] and thin films [58] were all synthesized using the same colloidal silica nanoparticles and had similar structures based on the reported TEM images and nitrogen adsorption–desorption
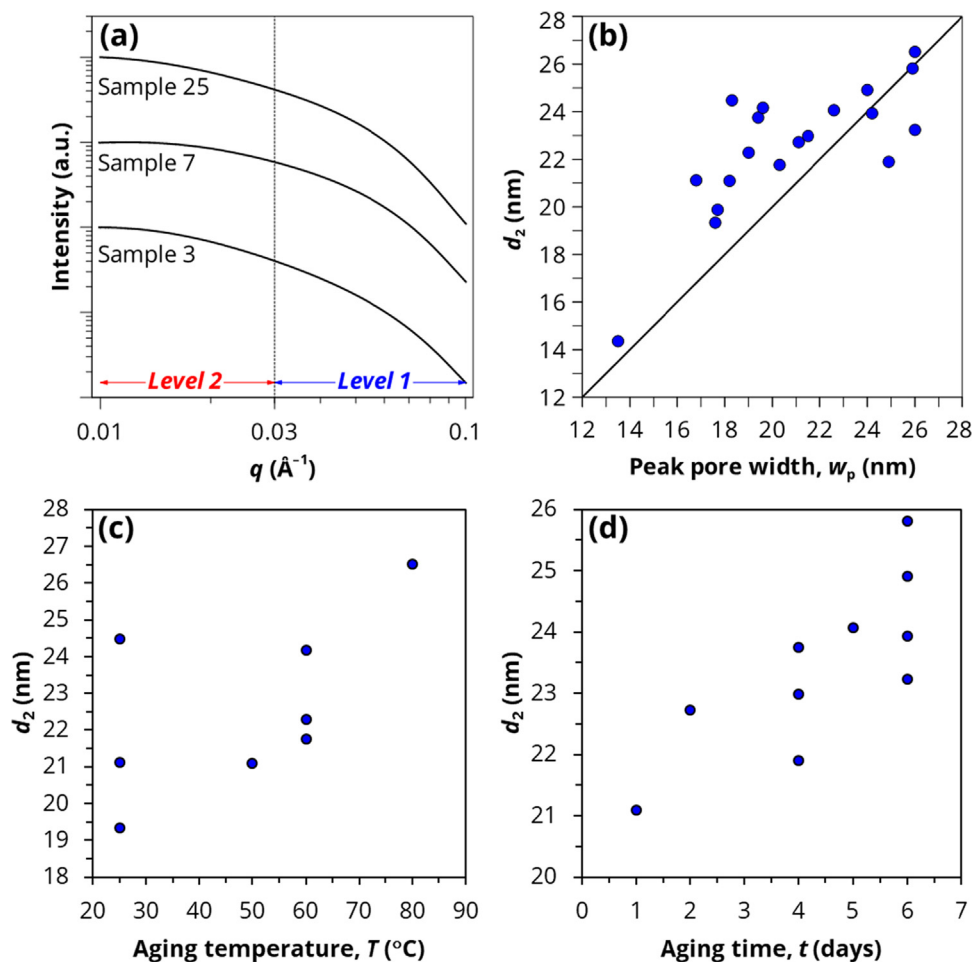

Fig. 7. (a) Small-angle X-ray scattering patterns of nanoparticle-based silica aerogel monoliths synthesized on omniphobic substrates and aged using different conditions (Scheme 1) namely Sample 3 synthesized on PTFE and aged at room temperature for 1 day, Sample 7 synthesized on PTFE and aged at 40 °C for 3 days, and Sample 25 synthesized on PTFE and aged at 80 °C for 1 day. (b-d) Diameter d_2 of the Level 2 scatterers as a function of (b) the peak pore width w_p for the present nanoparticle-based silica aerogels, (c) aging temperature T for aerogels aged for 1 day, and (d) aging time t for aerogels aged at 50 °C (see Table 1). Labels Level 1 and Level 2 in (a) indicate ranges where two levels of the Guinier-Porod fit were applied to extract Porod exponents P_1 and P_2 and gyration radii R_{g1} and R_{g2} (see Table S1). The solid line in (b) represents $d_2 = w_p$.
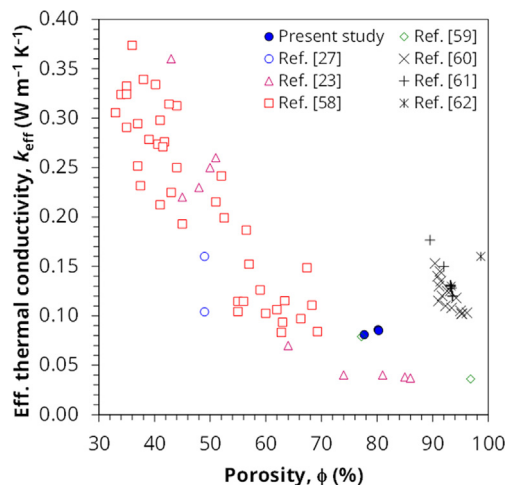
Fig. 8. Effective thermal conductivity k_{eff} as a function of porosity ϕ for (i) nanoparticle-based silica aerogel slabs (present study), (ii) nanoparticle-based mesoporous silica slabs [27], (iii) nanoparticle-based mesoporous silica thin films [58], (iv) hydrophobic TEOS-based silica aerogels dried at ambient pressure [23,59,60], (v) hydrophobic sodium silicate-based silica aerogels dried at ambient pressure [61], (vi) and hydrophobic and hydrophilic TMOS-based silica aerogels dried using supercritical CO_2 [62].

isotherms [27,58]. Note, however, that the mesoporous thin films were synthesized using triblock copolymers as pore templates to better control their porosity [58]. Finally, silica aerogels investigated in Refs. [59–62] with porosity ϕ > 90% were synthesized using molecular precursors, such as TMOS, TEOS, and sodium silicate. Some of these aerogels were also reacted with trimethylchlorosilane or hexamethyldisilazane to induce hydrophobic properties [23,59–62].

Fig. 8 indicates that thanks to the increased porosity achieved by the combination of aging, solvent exchange, and ambient drying, the present aerogels had larger porosities ($\phi \approx 80\%$) and lower effective thermal conductivities than our previously synthesized nanoparticle-based mesoporous silica slabs and films [27,58]. Interestingly, the present pure silica aerogels were found to have thermal conductivities lower than that of many optically-transparent silica aerogels despite their lower porosities [60–62]. However, their thermal conductivities were higher than those of our recently published optically-transparent ambigels despite having similar porosity [23] and of other (albeit organosilica) aerogels reported in the literature [25,26,63]. These differences were likely due to differences in the fractal dimension of the different aerogels, as theoretically predicted [64] and experimentally confirmed [23]. Indeed, for a given porosity, aerogels with larger fractal dimension have lower thermal conductivities due to their branched and interconnected structure. In fact, the present nanoparticle-based aerogels had mass fractal dimension D_m of 1.0–1.4 (see Table S1) while our precursor-based ambigel slabs [23] featured D_m of 2.3–2.6.

3.5. Hydrophobic properties

The as-synthesized nanoparticle-based aerogel slabs were hydrophilic and crumbled upon contact with water. This structural failure was due to rapid infiltration of water in the mesopores resulting in significant stress on the pore walls due to the relatively large surface tension of the air/water interface. It is important that transparent aerogels for window insulation, solar-thermal energy conversion systems, and other applications of interest resist degradation by water as they are normally exposed to the elements such as rain and humid air. Therefore, the as-synthesized aerogels were
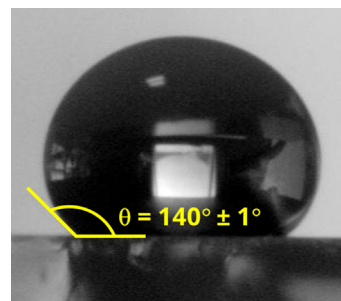

Fig. 9. Optical image of a water droplet on a hydrophobic nanoparticle-based silica aerogel.

exposed to TMCS vapor to induce hydrophobicity and to prevent water infiltration. Fig. 9 shows an optical image of a water droplet on a hydrophobic nanoparticle-based silica aerogel monolith with an average water contact angle θ = 140° ± 1°. Notably, the hydrophobic aerogel slabs were as transparent as the as-synthesized slabs indicating that modification with TMCS did not affect their optical properties.

Overall, these results indicate that the present nanoparticle-based silica aerogel monoliths are good candidates for optically transparent thermally insulating materials. Indeed, they offer similar or smaller thermal conductivity and larger visible transmittance than other aerogels reported for this application [54,60–62] while the synthesis process at ambient conditions is intrinsically scalable and comparatively inexpensive. In addition, unlike aerogels with porosities exceeding 95% [65], the resulting slabs were mechanically sturdy and could be handled by hand. They could also be made hydrophobic and bonded to a flat glass sheet with a UV-curing adhesive and were resistant to deterioration in UV light (see Supplementary material), thus facilitating their integration in transparent and thermally insulating composite materials or structures for window solutions.

4. Conclusion

This paper presented a novel sol-gel method to synthesize thick, large, and highly porous yet transparent silica aerogel monoliths from suspensions of silica nanoparticles and dried under ambient conditions. The synthesis combined the following strategies (i) use of omniphobic substrates to reduce stress during gelation and drying and achieve optically smooth surfaces, (ii) fast gelation of a colloidal solution by adjusting its pH, (iii) accelerated aging at elevated temperatures to reinforce the silica network, and (iv) exchange of water within the pores with a low surface tension solvent to reduce capillary forces during ambient drying and achieve large porosity (70–80%). The synthesized transparent nanoparticle-based silica aerogel monoliths had thicknesses up to 5 mm, diameters up to 10 cm, porosities exceeding 80%, and effective thermal conductivities as low as 0.081 W m^{-1} K^{-1}. In addition, the slabs had visible transmittance exceeding 75% even for slabs as thick as 5 mm. They could be easily made hydrophobic and were sufficiently strong to be handled by hand and adhered to a glass substrate with UV curing adhesive. The aging duration and temperature and number and amount of solvent exchange, need to be optimized to minimize the processing time and environmental impact of the synthesis method.

CRediT authorship contribution statement

Michal Marszewski: Conceptualization, Methodology, Formal analysis, Data curation, Visualization, Writing – original draft.

Sophia C. King: Resources, Investigation, Formal analysis, Validation. **Tiphaine Galy:** Investigation, Formal analysis, Data curation. **Glareh N. Kashanchi:** Resources, Investigation, Formal analysis, Data curation, Validation. **Ali Dashti:** Investigation, Formal analysis, Data curation. **Yan Yan:** Investigation, Formal analysis, Data curation. **Man Li:** Investigation, Formal analysis, Data curation. **Danielle M. Butts:** Resources, Investigation, Data curation. **Patricia E. McNeil:** Resources, Investigation, Formal analysis, Data curation. **Esther Lan:** Resources, Investigation. **Bruce Dunn:** Methodology, Supervision, Funding acquisition. **Yongjie Hu:** Methodology, Supervision, Funding acquisition. **Sarah H. Tolbert:** Methodology, Supervision, Funding acquisition. **Laurent Pilon:** Conceptualization, Methodology, Formal analysis, Project administration, Supervision, Writing – review & editing, Funding acquisition.

Declaration of Competing Interest

The authors declare that they have no known competing financial interests or personal relationships that could have appeared to influence the work reported in this paper.

Acknowledgment

Appendix A. Supplementary material

Supplementary data to this article can be found online at https://doi.org/10.1016/j.jcis.2021.07.159.

References

[1] N. Hüsing, U. Schubert, Aerogels—airy materials: chemistry, structure, and properties, Angew. Chem. Int. Ed. 37 (1998) 22–45, https://doi.org/10.1002/(SICI)1521-3773(19980202)37:1/2<22::AID-ANIE22>3.0.CO;2-I.

[2] A.C. Pierre, G.M. Pajonk, Chemistry of aerogels and their applications, Chem. Rev. 102 (2002) 4243–4266, https://doi.org/10.1021/cr0101306.

[3] M.A. Aegerter, N. Leventis, M.A. Koebel (Eds.), Aerogels handbook, Springer, New York, 2011.

[4] A. Nordgaard, W. Beckman, Modeling of flat-plate collectors based on monolithic silica aerogel, Sol. Energy. 49 (1992) 387–402, https://doi.org/10.1016/0038-092X(92)90111-M.

[5] L.A. Weinstein, J. Loomis, B. Bhatia, D.M. Bierman, E.N. Wang, G. Chen, Concentrating solar power, Chem. Rev. 115 (2015) 12797–12838, https://doi.org/10.1021/acs.chemrev.5b00397.

[6] K. McEnaney, L. Weinstein, D. Kraemer, H. Ghasemi, G. Chen, Aerogel-based solar thermal receivers, Nano Energy. 40 (2017) 180–186, https://doi.org/10.1016/j.nanoen.2017.08.006.

[7] E. Strobach, B. Bhatia, S. Yang, L. Zhao, E.N. Wang, High temperature annealing for structural optimization of silica aerogels in solar thermal applications, J. Non-Cryst. Solids. 462 (2017) 72–77, https://doi.org/10.1016/j.jnoncrysol.2017.02.009.

[8] L. Zhao, B. Bhatia, S. Yang, E. Strobach, L.A. Weinstein, T.A. Cooper, G. Chen, E.N. Wang, Harnessing heat beyond 200 °C from unconcentrated sunlight with nonevacuated transparent aerogels, ACS Nano. 13 (2019) 7508–7516, https://doi.org/10.1021/acsnano.9b02976.

[9] V. Wittwer, Development of aerogel windows, J. Non-Cryst. Solids. 145 (1992) 233–236, https://doi.org/10.1016/S0022-3093(05)80462-4.

[10] K.I. Jensen, J.M. Schultz, F.H. Kristiansen, Development of windows based on highly insulating aerogel glazings, J. Non-Cryst. Solids. 350 (2004) 351–357, https://doi.org/10.1016/j.jnoncrysol.2004.06.047.

[11] M. Schmidt, G. Boettger, M. Eich, W. Morgenroth, U. Huebner, R. Boucher, H.G. Meyer, D. Konjhodzic, H. Bretinger, F. Marlow, Ultralow refractive index substrates–a base for photonic crystal slab waveguides, Appl. Phys. Lett. 85 (2004) 16–18, https://doi.org/10.1063/1.1767962.

[12] S. Murai, K. Fujita, K. Nakanishi, K. Hirao, Fabrication of dye-infiltrated macroporous silica for laser amplification, J. Non-Cryst. Solids. 345–346 (2004) 438–442, https://doi.org/10.1016/j.jnoncrysol.2004.08.059.

[13] C.J. Brinker, G.W. Scherer, Sol-Gel Science: The Physics and Chemistry of Sol-Gel Processing, Academic Press, Boston, 1990.

[14] J.R. Rumble, ed., CRC handbook of chemistry and physics, in: 98th edition 2017-2018, CRC Press, Taylor & Francis Group, New York, 2017.

[15] T. Burger, J. Fricke, Aerogels: Production, modification and applications, Berichte Bunsenges. Für Phys. Chem. 102 (1998) 1523–1528, https://doi.org/10.1002/bbpc.19981021102.

[16] C.J. Lee, G.S. Kim, S.H. Hyun, Synthesis of silica aerogels from waterglass via new modified ambient drying, J. Mater. Sci. 37 (2002) 2237–2241, https://doi.org/10.1023/A:1015309014546.

[17] S.D. Bhagat, C.-S. Oh, Y.-H. Kim, Y.-S. Ahn, J.-G. Yeo, Methyltrimethoxysilane based monolithic silica aerogels via ambient pressure drying, Microporous Mesoporous Mater. 100 (2007) 350–355, https://doi.org/10.1016/j.micromeso.2006.10.026.

[18] A.P. Rao, A.V. Rao, G.M. Pajonk, Hydrophobic and physical properties of the ambient pressure dried silica aerogels with sodium silicate precursor using various surface modification agents, Appl. Surf. Sci. 253 (2007) 6032–6040, https://doi.org/10.1016/j.apsusc.2006.12.117.

[19] S.-W. Hwang, H.-H. Jung, S.-H. Hyun, Y.-S. Ahn, Effective preparation of crack-free silica aerogels via ambient drying, J. Sol-Gel Sci. Technol. 41 (2007) 139–146, https://doi.org/10.1007/s10971-006-0513-y.

[20] T.-Y. Wei, S.-Y. Lu, Y.-C. Chang, Transparent, hydrophobic composite aerogels with high mechanical strength and low high-temperature thermal conductivities, J. Phys. Chem. B. 112 (2008) 11881–11886, https://doi.org/10.1021/jp804855v.

[21] J.L. Gurav, A.V. Rao, D.Y. Nadargi, H.-H. Park, Ambient pressure dried TEOS-based silica aerogels: good absorbents of organic liquids, J. Mater. Sci. 45 (2010) 503–510, https://doi.org/10.1007/s10853-009-3968-8.

[22] I.-K. Jung, J.L. Gurav, T.-J. Ha, S.G. Choi, S. Baek, H.-H. Park, The properties of silica aerogels hybridized with SiO2 nanoparticles by ambient pressure drying, Ceram. Int. 38 (2012) S105–S108, https://doi.org/10.1016/j.ceramint.2011.04.060.

[23] D.M. Butts, P.E. McNeil, M. Marszewski, E. Lan, T. Galy, M. Li, J.S. Kang, D. Ashby, S. King, S.H. Tolbert, Y. Hu, L. Pilon, B.S. Dunn, Engineering mesoporous silica for superior optical and thermal properties, MRS Energy Sustain. 7 (2020) 39, https://doi.org/10.1557/mre.2020.40.

[24] G. Zu, T. Shimizu, K. Kanamori, Y. Zhu, A. Maeno, H. Kaji, J. Shen, K. Nakanishi, Transparent, superflexible doubly cross-linked polyvinylpolymethylsiloxane aerogel superinsulators via ambient pressure drying, ACS Nano. 12 (2018) 521–532, https://doi.org/10.1021/acsnano.7b07117.

[25] G. Zu, K. Kanamori, T. Shimizu, Y. Zhu, A. Maeno, H. Kaji, K. Nakanishi, J. Shen, Versatile double-cross-linking approach to transparent, machinable, supercompressible, highly bendable aerogel thermal superinsulators, Chem. Mater. 30 (2018) 2759–2770, https://doi.org/10.1021/acs.chemmater.8b00563.

[26] Z. Niu, X. He, T. Huang, B. Tang, X. Cheng, Y. Zhang, Z. Shao, A facile preparation of transparent methyltriethoxysilane based silica xerogel monoliths at ambient pressure drying, Microporous Mesoporous Mater. 286 (2019) 98–104, https://doi.org/10.1016/j.micromeso.2019.05.036.

[27] M. Marszewski, S.C. King, Y. Yan, T. Galy, M. Li, A. Dashti, D.M. Butts, J.S. Kang, P.E. McNeil, E. Lan, B. Dunn, Y. Hu, S.H. Tolbert, L. Pilon, Thick transparent nanoparticle-based mesoporous silica monolithic slabs for thermally insulating window materials, ACS Appl. Nano Mater. 2 (2019) 4547–4555, https://doi.org/10.1021/acsanm.9b00903.

[28] Krytox Performance Lubricants Product Information Datasheet, n.d.

[29] 3MTM FluorinertTM Electronic Liquid FC-70 Product Information Datasheet, n.d.

[30] Perfluoro(tetradecahydrophenanthrene) Safety Data Sheet 1200214, n.d.

[31] C.A. Schneider, W.S. Rasband, K.W. Eliceiri, NIH Image to ImageJ: 25 years of image analysis, Nat. Methods. 9 (2012) 671–675, https://doi.org/10.1038/nmeth.2089.

[32] S. Brunauer, P.H. Emmett, E. Teller, Adsorption of gases in multimolecular layers, J. Am. Chem. Soc. 60 (1938) 309–319, https://doi.org/10.1021/ja01269a023.

[33] M. Kruk, M. Jaroniec, Gas adsorption characterization of ordered organic−inorganic nanocomposite materials, Chem. Mater. 13 (2001) 3169–3183, https://doi.org/10.1021/cm0101069.

[34] H. Naono, M. Hakuman, T. Shiono, Analysis of nitrogen adsorption isotherms for a series of porous silicas with uniform and cylindrical pores: A new method of calculating pore size distribution of pore radius 1–2 nm, J. Colloid Interface Sci. 186 (1997) 360–368, https://doi.org/10.1006/jcis.1996.4677.

[35] J. Rouquerol, F. Rouquerol, P. Llewellyn, G. Maurin, K.S.W. Sing, Adsorption by Powders and Porous Solids: Principles, Methodology and Applications, 2nd edition., Academic Press, Amsterdam, The Netherlands, 2013.

[36] M. Kruk, M. Jaroniec, A. Sayari, Application of large pore MCM-41 molecular sieves to improve pore size analysis using nitrogen adsorption measurements, Langmuir. 13 (1997) 6267–6273, https://doi.org/10.1021/la970776m.

[37] E.P. Barrett, L.G. Joyner, P.P. Halenda, The determination of pore volume and area distributions in porous substances. I. Computations from nitrogen isotherms, J. Am. Chem. Soc. 73 (1951) 373–380, https://doi.org/10.1021/ja01145a126.

[38] M. Jaroniec, M. Kruk, J.P. Olivier, Standard nitrogen adsorption data for characterization of nanoporous silicas, Langmuir. 15 (1999) 5410–5413, https://doi.org/10.1021/la990136e.

[39] M. Jaroniec, Evaluation of the fractal dimension from a single adsorption isotherm, Langmuir. 11 (1995) 2316–2317, https://doi.org/10.1021/la00006a076.

[40] J. Ilavsky, Nika: software for two-dimensional data reduction, J. Appl. Crystallogr. 45 (2012) 324–328, https://doi.org/10.1107/S0021889812004037.

[41] J. Ilavsky, P.R. Jemian, Irena: tool suite for modeling and analysis of small-angle scattering, J. Appl. Crystallogr. 42 (2009) 347–353, https://doi.org/10.1107/S0021889809002222.

[42] G. Beaucage, Approximations leading to a unified exponential/power-law approach to small-angle scattering, J. Appl. Crystallogr. 28 (1995) 717–728, https://doi.org/10.1107/S0021889895005292.

[43] G. Beaucage, Small-angle scattering from polymeric mass fractals of arbitrary mass-fractal dimension, J. Appl. Crystallogr. 29 (1996) 134–146, https://doi.org/10.1107/S0021889896011605.

[44] G. Beaucage, S. Rane, S. Sukumaran, M.M. Satkowski, L.A. Schechtman, Y. Doi, Persistence Length of Isotactic Poly(hydroxy butyrate), Macromolecules. 30 (1997) 4158–4162, https://doi.org/10.1021/ma970373t.

[45] ASTM D1003-13, Standard Test Method for Haze and Luminous Transmittance of Transparent Plastics, ASTM International, West Conshohocken, PA, 2013. https://doi.org/10.1520/D1003-13.

[46] R.W.G. Hunt, The reproduction of colour, 6th ed., John Wiley & Sons, Hoboken, NJ, 2004.

[47] NFRC 300-2014, Test Method for Determining the Solar Optical Properties of Glazing Materials and Systems, National Fenestration Rating Council, Greenbelt, MD, 2013. https://www.nfrccommunity.org/store/ViewProduct.aspx?id=1402242 (accessed October 19, 2020).

[48] BS EN 410:2011, Glass in building. Determination of luminous and solar characteristics of glazing, British Standards Institution, London, United Kingdom, 2011.

[49] M.K. Gunde, U.O. Krašovec, W.J. Platzer, Color rendering properties of interior lighting influenced by a switchable window, JOSA A. 22 (2005) 416–423, https://doi.org/10.1364/JOSAA.22.000416.

[50] R. Dangol, T. Kruisselbrink, A. Rosemann, Effect of Window Glazing on Colour Quality of Transmitted Daylight, J. Daylighting. 4 (2017) 37–47, https://doi.org/10.15627/jd.2017.6.

[51] A. Ricklefs, A.M. Thiele, G. Falzone, G. Sant, L. Pilon, Thermal conductivity of cementitious composites containing microencapsulated phase change materials, Int. J. Heat Mass Transf. 104 (2017) 71–82, https://doi.org/10.1016/j.ijheatmasstransfer.2016.08.013.

[52] ASTM C177-19, Standard Test Method for Steady-State Heat Flux Measurements and Thermal Transmission Properties by Means of the Guarded-Hot-Plate Apparatus, ASTM International, West Conshohocken, PA, 2019. https://doi.org/10.1520/C0177-19

[53] J.H. Harreld, W. Dong, B. Dunn, Ambient pressure synthesis of aerogel-like vanadium oxide and molybdenum oxide, Mater. Res. Bull. 33 (1998) 561–567, https://doi.org/10.1016/S0025-5408(98)00022-1.

[54] L. Zhao, S. Yang, B. Bhatia, E. Strobach, E.N. Wang, Modeling silica aerogel optical performance by determining its radiative properties, AIP Adv. 6 (2016), https://doi.org/10.1063/1.4943215 025123.

[55] T. Galy, D. Mu, M. Marszewski, L. Pilon, Computer-generated mesoporous materials and associated structural characterization, Comput. Mater. Sci. 157 (2019) 156–167, https://doi.org/10.1016/j.commatsci.2018.10.035.

[56] K.S.W. Sing, D.H. Everett, R.A.W. Haul, L. Moscou, R.A. Pierotti, J. Rouquerol, T. Siemieniewska, Reporting physisorption data for gas, solid systems with special reference to the determination of surface area and porosity (Recommendations 1984), Pure Appl. Chem. 57 (1985) 603–619, https://doi.org/10.1351/pac198557040603.

[57] M. Thommes, K. Kaneko, A.V. Neimark, J.P. Olivier, F. Rodriguez-Reinoso, J. Rouquerol, K.S.W. Sing, Physisorption of gases, with special reference to the evaluation of surface area and pore size distribution (IUPAC Technical Report), Pure Appl. Chem. 87 (2015) 1051–1069, https://doi.org/10.1515/pac-2014-1117.

[58] Y. Yan, S.C. King, M. Li, T. Galy, M. Marszewski, J.S. Kang, L. Pilon, Y. Hu, S.H. Tolbert, Exploring the effect of porous structure on thermal conductivity in templated mesoporous silica films, J. Phys. Chem. C. 123 (2019) 21721–21730, https://doi.org/10.1021/acs.jpcc.9b03767.

[59] T.-Y. Wei, T.-F. Chang, S.-Y. Lu, Y.-C. Chang, Preparation of monolithic silica aerogel of low thermal conductivity by ambient pressure drying, J. Am. Ceram. Soc. 90 (2007) 2003–2007, https://doi.org/10.1111/j.1551-2916.2007.01671.x.

[60] A.P. Rao, G.M. Pajonk, A.V. Rao, Effect of preparation conditions on the physical and hydrophobic properties of two step processed ambient pressure dried silica aerogels, J. Mater. Sci. 40 (2005) 3481–3489, https://doi.org/10.1007/s10853-005-2853-3.

[61] U.K.H. Bangi, I.-K. Jung, C.-S. Park, S. Baek, H.-H. Park, Optically transparent silica aerogels based on sodium silicate by a two step sol–gel process and ambient pressure drying, Solid State Sci. 18 (2013) 50–57, https://doi.org/10.1016/j.solidstatesciences.2012.12.016.

[62] A.A. Günay, H. Kim, N. Nagarajan, M. Lopez, R. Kantharaj, A. Alsaati, A. Marconnet, A. Lenert, N. Miljkovic, Optically transparent thermally insulating silica aerogels for solar thermal insulation, ACS Appl. Mater. Interfaces. 10 (2018) 12603–12611, https://doi.org/10.1021/acsami.7b18856.

[63] T. Shimizu, K. Kanamori, A. Maeno, H. Kaji, C.M. Doherty, P. Falcaro, K. Nakanishi, Transparent, highly insulating polyethyl- and polyvinylsilsesquioxane aerogels: mechanical improvements by vulcanization for ambient pressure drying, Chem. Mater. 28 (2016) 6860–6868, https://doi.org/10.1021/acs.chemmater.6b01936.

[64] A. Emmerling, J. Fricke, Scaling properties and structure of aerogels, J. Sol-Gel Sci. Technol. 8 (1997) 781–788, https://doi.org/10.1023/A:1018381923413.

[65] J.P. Randall, M.A.B. Meador, S.C. Jana, Tailoring mechanical properties of aerogels for aerospace applications, ACS Appl. Mater. Interfaces. 3 (2011) 613–626, https://doi.org/10.1021/am200007n.